

Contents

Introduction	3
1 Theoretical Background	7
Micro/Meso-scopic model	8
1.1 Gross-Pitaevskii model	8
1.2 Quantum vortex	9
1.3 Vortex filament model	10
1.4 Vortex dynamics	11
Macroscopic model	14
1.5 Hydrodynamics of superfluid	14
1.6 Oscillatory motion in superfluid Helium-II	17
1.7 Quantum turbulence	19
2 Experimental Approach	20
2.1 Apparatus	20
2.2 Generation of QT	21
2.3 Measurement methods and Processing	23
3 Simulations	25
3.1 Vortex filament model	25
3.2 Time evolution	30
3.3 Re-segmentation of vortex	31
3.4 Future implementations	32

4 Results (15 pgs)	35
4.1 Drag force graphs	35
4.2 Universal Scaling	35
4.3 Flow phase diagram	36
4.4 Simulation experiments	36
4.5 Vortex ring	37
5 Conclusions (2 pgs)	45
6 Appendix	46
Bibliography	49

Introduction (3 pgs)

The liquid state of ${}^4\text{He}$ exists in two phases:

- Helium I - a high temperature phase ($2.17\text{ K} < T < 4.2\text{ K}$)
- Helium II - a low temperature phase ($T < 2.17\text{ K}$)

These two phases are connected with the *lambda transition*, which occurs at the critical temperature $T_\lambda = 2.17\text{ K}$ at saturated vapour pressure. Helium I is a classical fluid described by ordinary Navier-Stokes (N-S) equations, whereas Helium II indicates the Bose-Einstein condensate (superfluid) in much more way.

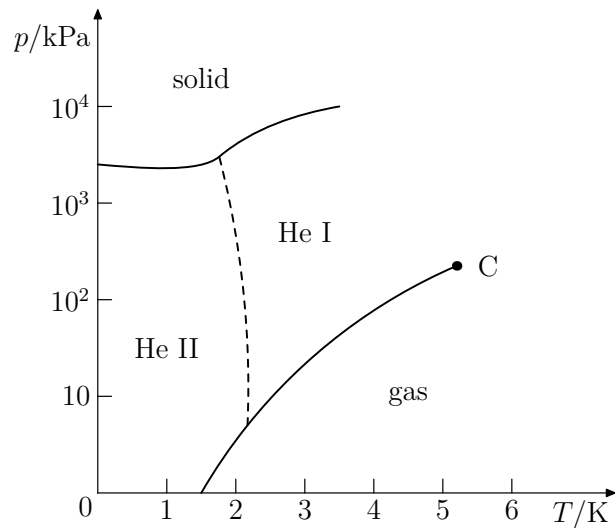


Figure 1: Pressure-Temperature diagram of Helium

A simple, phenomenological model of the Helium II motion was proposed by Tisza and Landau - the *two-fluid model*. Within this model, Helium II is depicted as a mixture of two interpenetrating fluid components:

- normal component - density ρ_n , velocity field \mathbf{v}_n , ordinary viscous N-S equation of motion, carrying entropy and thermal excitations represented by *phonons* and *rotons*
- superfluid component - density ρ_s , velocity field \mathbf{v}_s , modified Euler equation (without viscosity) of motion by quantum terms, no entropy, represented by macroscopic wave function

The total density of Helium II sums up to $\rho = \rho_n + \rho_s$ and the relative proportion of normal/superfluid component is determined by the temperature. Near $T \rightarrow 0$ Helium II becomes entirely superfluid $\rho_s/\rho \rightarrow 1$. The temperature dependence of this ratio is highly nonlinear. For example, the ratio ρ_n/ρ drops from 100% at 2.17 K to 50% at 1.95 K, to < 5% at 1.3 K, and is effectively negligible under 1 K.

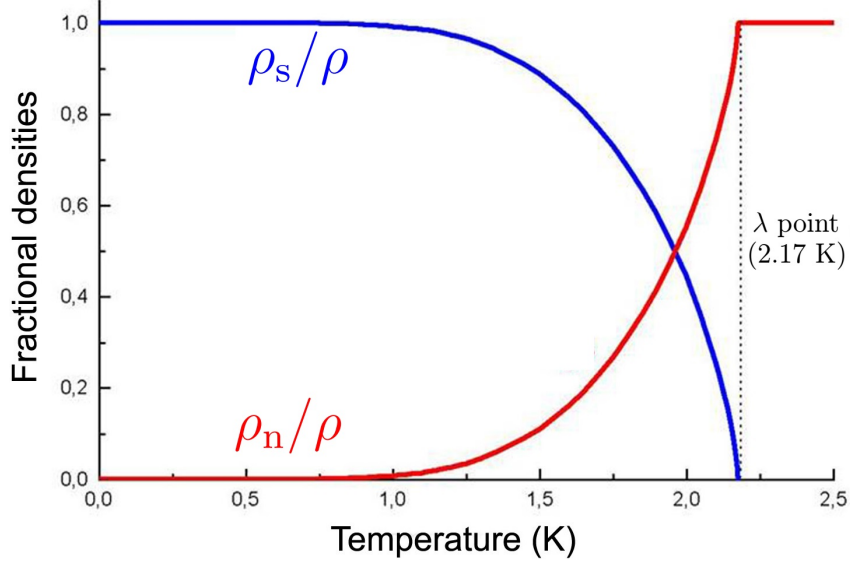


Figure 2: Temperature dependence of two-fluid density proportions

The two-fluid model explains many observed phenomena - among other we pick *second sound* and *thermal counterflow* due to their importance in the study of turbulence.

Second sound: Ordinary sound (the wave of density ρ and pressure P) in Helium II is called *first sound*. In such process, temperature T and entropy S is conserved and \mathbf{v}_n and \mathbf{v}_s oscillate in phase with each others. On the contrary, a second sound is an antiphase oscillation of \mathbf{v}_n and \mathbf{v}_s , causing the oscillation of T and S while ρ and P are constant. In this work, the second sound phenomenon is used for detection of quantized vortices, which naturally appear within Helium II.

Thermal counterflow: Helium II is able to transfer heat in a special way. Let's consider a closed channel filled with Helium II and a dissipating resistor localised at one end of the channel. In normal fluid, the heat is transferred away from the resistor by conduction and convection mechanism. However, in Helium II the heat is carried away only by the normal component. To conserve the total mass flux, some superfluid fluid flow toward the resistor. In this way, a counterflow is generated. If the counterflow is strong enough, the superfluid turbulence is generated.

It arises from the quantum nature of superfluid, that such fluid should not perform any rotation. It is called then *irrotational*. However, when Helium II rotates or moves faster

than a critical velocity, the circulation is *quantized* and so-called *quantized vortices* are created, which makes the hydrodynamics of Helium II particularly interesting. The vortex nucleation process is still a subject of many current investigations. Superfluid vortex lines can be spatially organized (laminar flows) or completely disorganized (turbulent flows).

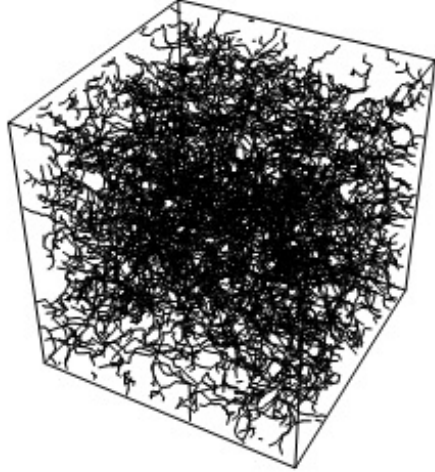


Figure 3: small simulation cube of tangle of quantum vortices??

It has only recently been realized that helium II is an attractive candidate for investigating classical turbulence (CT) problems. Quantum turbulence (QT) can be achieved in many traditional ways - driving a mass flow, spinning discs, oscillating grids and forks, ultrasound, jets. Considering all these methods together, the general trend is that the slow, laminar flow of Helium II (with or without vortices) tends to be rather different from the classical fluid flow. In case of fast motion, the turbulent Helium II seems to behave similar to classical turbulent flow.

To characterize the turbulence we use the dimensionless Reynolds number. Examples of the observed classical features of Helium II QT (regardless on temperature) were found during experiments with flow strength of $\text{Re} \approx 10^6$ (pressure drops)??, of $\text{Re} \approx 10^5$ (sphere drag crisis)??, of $\text{Re} \approx 4 \times 10^4$ (whole fluid vorticity)?? and of $\text{Re} \approx 4 \times 10^3$ (structures of turbulence)??.

In classical fluid dynamics (solutions of motion equations), one of the useful tools for understanding the geometry and dynamics of flow is *vortex filament model*. With the rapid development of available computational power, large simulations have become the methods of choice for calculating the motion of fluids. In superfluids like Helium II, due to the quantization of circulation, vorticity can only exist within vortex filaments with a certain core size, which makes the model a way more applicable than in fields of classical fluids.

Motivations and Goals

Motivations:

- ivestigate transition from CT to QT at various temperatures
- prepare clear and reusable codebase for QT simulation
- ??

Goals:

- prepare superfluid Helium II and subsequently generate and detect second sound
- generate QT with an oscillating object and measure attenuations
- simulate qunatum vortex rings and compare its properties with the theoretical ones

Motivations: investigate critical velocities and vortex density, create numeric model

Goals: measure hydrodynamic profiles for more temperatures with oscillating object, transition from CT to QT, investifate numerically vortex rings

1. Theoretical Background

The theoretical part of this Thesis is composed of two chapters:

1. Mesoscopic view - theoretically cover London's theory, creation and numerical modelling of quantum vortex, vortex dynamics.
3. Macroscopic view - hydrodynamics of two-fluid model, oscillatory motion in such fluid, creation of QT, existence and usage of second sound

The aim of this part of thesis is to introduce the basic properties of quantized vortex lines in Helium II and summarize the state of the art knowledge of superfluid turbulence. Then there is discussed the theoretical methods used to study quantized vorticity, quantum turbulence and the results obtained using such methods.

Micro/Meso-scopic view

One of the most useful ways of describing superfluid helium at $T = 0$ starts with nonlinear Schrodinger equation (NLSE) for the one-particle wave function ψ . Since the superfluid helium is a strongly correlated system dominated by collective effects, this imperfect Bose-Einstein condensate (BEC) is approximately described by Gross-Pitaevskii equation. Although, it must be noted that the real Helium II is a dense fluid, not a weakly interacting Bose gas described by NLSE.

1.1 Gross-Pitaevskii model

In terms of single-particle wavefunction $\psi(\mathbf{r}, t)$:

$$i\hbar \frac{\partial \psi}{\partial t} = -\frac{\hbar^2}{2m} \nabla^2 \psi + \psi \int |\psi(\mathbf{r}', t)|^2 V(|\mathbf{r} - \mathbf{r}'|) d\mathbf{r}', \quad (1.1)$$

where $V(|\mathbf{r} - \mathbf{r}'|)$ is the potential of two-body interaction between bosons. The normalization is set as $\int |\psi|^2 d\mathbf{r} = N$, where N is number of bosons. By replacing potential with repulsive δ -function of strength V_0 one obtains:

$$i\hbar \frac{\partial \Psi}{\partial t} = -\frac{\hbar^2}{2m} \nabla^2 \Psi - m\varepsilon \Psi + V_0 |\Psi|^2 \Psi, \quad (1.2)$$

where ε is the energy per unit mass and $\Psi = A e^{i\Phi}$ is a macroscopic wave function of condensate. In this way one can define the condensate's density $\rho_{BEC} = m\Psi\Psi^* = mA^2$ and velocity $\mathbf{v}_{BEC} = (\hbar/m)\nabla\Psi$. Note that equation (1.2) is equivalent to a continuity equation and an modified Euler equation (by the so called quantum pressure term).

Even though the superfluid is irrotational $\omega = \nabla \times \mathbf{v}_{BEC} = \mathbf{0}$, the NLSE has a vortex-like solution: $\mathbf{v}_s = \varkappa/2\pi r \mathbf{e}_\theta$, where θ is the azimuthal angle and $\varkappa = 9.97 \times 10^{-4} \text{ cm}^2 \cdot \text{s}^{-1}$ is the *quantum of circulation*, obtained from:

$$\varkappa = \oint_C \mathbf{v}_{BEC} \cdot d\ell = \frac{\hbar}{m} \quad (1.3)$$

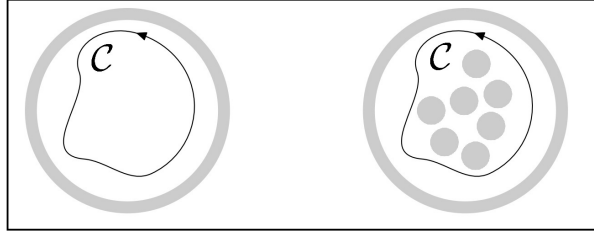


Figure 1.1: topological singularities within superfluid

1.2 Quantum vortex

Superfluid vortex lines appear when helium II moves faster than a certain critical velocity. Such *nucleation* is the subject of many investigations and described widely later in this work.

The simplest way to create quantum vortices is to rotate cylinder with superfluid Helium II with high enough angular velocity Ω . Created vortex lines form an ordered array of density $L = 2\Omega/\kappa$, all aligned along the axis of rotation. *Vortex line density* L can be also interpreted as a total vortex length in an unit volume.

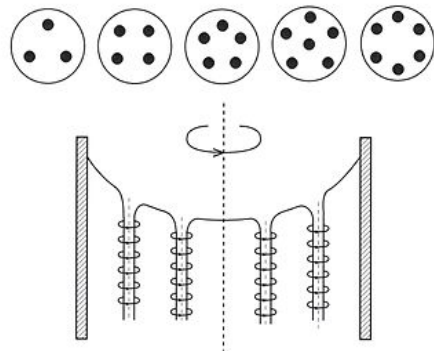


Figure 1.2: Array of quantized vortices in a rotating container

The key properties of Onsager-Feynman vortex are the quantized circulation κ , superfluid rotational velocity field $\mathbf{v}_s = \kappa/2\pi r \mathbf{e}_\theta$ and the *vortex core parameter* a_0 . The core size a_0 can be estimated by substituting \mathbf{v}_s back into (1.2) and solving differential equation for ρ_s . One finds that ρ_s tends to the value $m^2\varepsilon/V_0$ for $r \rightarrow \infty$ and to zero density for $r \rightarrow 0$. The characteristic distance over which Ψ collapses (superfluid density ρ_s drops from bulk value to zero) is $a_0 \approx 10^{-10} \text{ m} = 1 \text{ \AA}$. From this, there is a conclusion that the vortex is hollow at its core and therefore, the topological defect occurs.

Taking a_0 as core radius, the energetical calculations showed that N quantum vortices contains more energy than N single quantum vortices. Hence it is generally assumed that only single quantum vortices are commonly observed.

Clearly, vortex lines don't have to be aligned in general. In most cases , the superfluid flow is strongly chaotic, better known as *quantum turbulence*. This topic is covered in more detail later in this work.

1.3 Vortex filament model

The vortex line can be represented as a curve via positional vector $\mathbf{s} = \mathbf{s}(\xi, t)$ in three-dimensional space. Here, ξ is arclength along the vortex line. Next we label \mathbf{s}' as $d\mathbf{s}/d\xi$ and \mathbf{s}'' as $d\mathbf{s}'/d\xi$. Within our context, \mathbf{s}' is a tangent vector and $|\mathbf{s}''|$ is a local curvature R^{-1} at a given point. The triad of vectors $\mathbf{s}', \mathbf{s}'', \mathbf{s}' \times \mathbf{s}''$ are perpendicular to each other and point along the tangent, normal and binormal respectively:

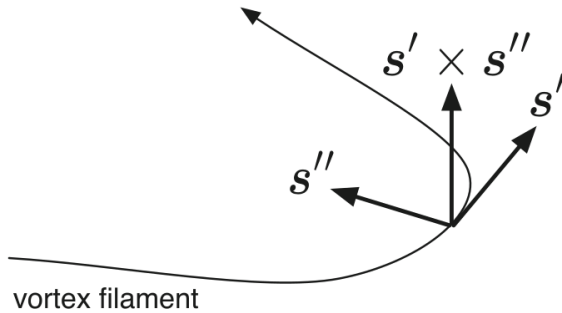


Figure 1.3: Schematic of the vortex filament and the triad vectors

We suppose that the superfluid component is incompressible $\nabla \cdot \mathbf{v}_s = 0$. Moreover, superfluid vorticity ω_s is localized only at positions of vortex filament $\omega_s(\mathbf{r}, t) = \nabla \times \mathbf{v}_s$. Combining these two properties gives the Poisson equation $\Delta \phi = \omega_s$ for the potential ϕ . Using Fourier transformation one obtains the Biot-Savart law for the superfluid velocity:

$$\mathbf{v}_s(\mathbf{r}) = \frac{\kappa}{4\pi} \int_{\mathcal{L}} \frac{(\mathbf{r}' - \mathbf{r}) \times d\mathbf{r}'}{|\mathbf{r}' - \mathbf{r}|^3}, \quad (1.4)$$

where the integral path \mathcal{L} represents curves along all vortex filaments.

This law determines the superfluid velocity field via the arrangement of the vortex filaments. Now we define the *self-induced* velocity \mathbf{v}_i , describing the motion which a vortex line induces onto itself due to its own curvature:

$$\mathbf{v}_i(\mathbf{s}) = \frac{\kappa}{4\pi} \int_{\mathcal{L}} \frac{(\mathbf{r}' - \mathbf{s}) \times d\mathbf{r}'}{|\mathbf{r}' - \mathbf{s}|^3} \quad (1.5)$$

However, this integral diverges as $\mathbf{r}' \rightarrow \mathbf{s}$ because the core structure of the quantized vortex was neglected. We avoid this divergence by splitting the integral into two parts - direct neighborhood of the point \mathbf{s} (local part) and the rest part \mathcal{L}' (nonlocal part). The Taylor expansion of the local part leads to finite result and thus:

$$\mathbf{v}_i(\mathbf{s}) = \mathbf{v}_{s,\text{local}} + \mathbf{v}_{s,\text{nonlocal}} \approx \beta \mathbf{s}' \times \mathbf{s}'' + \frac{\varkappa}{4\pi} \int_{\mathcal{L}'} \frac{(\mathbf{r}' - \mathbf{s}) \times d\mathbf{r}'}{|\mathbf{r}' - \mathbf{s}|^3}, \quad (1.6)$$

where $\beta = (\varkappa/4\pi) \ln(1/|\mathbf{s}'|a_0)$. This process is called Local Induction Approximation (LIA). Numerical study of Adachi et al. showed that the nonlocal term plays an important role even for homogeneous quantum turbulence.

Since there could be also external flow source of superfluid component, we define the total superfluid velocity, in laboratory frame, as:

$$\mathbf{v}_{s,tot} = \mathbf{v}_{s,ext} + \mathbf{v}_i \quad (1.7)$$

1.4 Vortex dynamics

To determine the equation of motion of \mathbf{s} we must recognize the forces acting upon the line - the magnus force \mathbf{f}_M and (at temperature $T > 0$), the drag force \mathbf{f}_D (both are per unit length).

The magnus force always arises when a rotating body moves in a flow. This emerges a pressure difference, which in our case of moving vortex line with circulation quantum \varkappa , exerts a force:

$$\mathbf{f}_M = \rho_s \varkappa \mathbf{s}' \times (\dot{\mathbf{s}} - \mathbf{v}_{s,tot}), \quad (1.8)$$

where $\dot{\mathbf{s}} = d\mathbf{s}/dt$ is the velocity of the line filament in the laboratory frame.

The drag force \mathbf{f}_D arises from the *mutual friction*, the interaction between the normal component and superfluid component. According to the findings of Vinen and Hall, the normal fluid flowing with velocity \mathbf{v}_n past a vortex core exerts a frictional force \mathbf{f}_D on the superfluid, given by:

$$\mathbf{f}_D = -\alpha(T) \rho_s \varkappa \mathbf{s}' \times [\mathbf{s}' \times (\mathbf{v}_n - \mathbf{v}_{s,tot})] - \alpha'(T) \varkappa \mathbf{s}' \times (\mathbf{v}_n - \mathbf{v}_{s,tot}) \quad (1.9)$$

The temperature dependent dimensionless parameters $\alpha(T)$ and $\alpha'(T)$ are written in terms of *mutual friction parameters* B and B' , which are known from experiments by Samuels and Donnelly:

$$\alpha(T) = \frac{\rho_n B(T)}{2\rho} \quad \alpha'(T) = \frac{\rho_n B'(T)}{2\rho} \quad (1.10)$$

The precise calculation of the mutual friction parameters over the entire temperature range is still an open problem. Although, we already know that in the area of high temperatures, the friction arises from the scattering process of rotons - an elementary excitation.

Since the mass of vortex core is usually neglected, the two forces \mathbf{f}_M and \mathbf{f}_D sum up into zero: $\mathbf{f}_M + \mathbf{f}_D = \mathbf{0}$. Hence, solving for $d\mathbf{s}/dt$, we obtain the Schwarz's equation:

$$\dot{\mathbf{s}} = \mathbf{v}_s + \mathbf{v}_i + \alpha \mathbf{s}' \times (\mathbf{v}_{ns} - \mathbf{v}_i) - \alpha' \mathbf{s}' \times [\mathbf{s}' \times (\mathbf{v}_{ns} - \mathbf{v}_i)], \quad (1.11)$$

where $\mathbf{v}_{ns} = \mathbf{v}_n - \mathbf{v}_s$ is the difference between the average velocity of normal fluid and the applied superfluid velocity.

On the basis of Schwarz's equation there can be developed an algorithm to numerically simulate vortex time evolution of an arbitrary configuration. More on this is written later in Simulation part of thesis.

Quantized vortex rings

A special case of vortex line configuration is a freely moving vortex ring. Such rings are usually created as a result of multi-vortex interconnection and have limited life expectancy. The exact expressions derived by classical hydrodynamics for the energy E_{ring} and center velocity v_{ring} , moving in a Helium II of density ρ and having a radius R much greater than its core radius $R \gg a_0$, are??

$$E_{\text{ring}} = \frac{1}{2} \kappa^2 \rho R \left(\ln(8R/a_0) - 2 + c \right) \quad (1.12)$$

$$v_{\text{ring}} = \frac{\kappa}{4\pi R} \left(\ln(8R/a_0) - 1 + c \right), \quad (1.13)$$

where c is a constant based on inner structure of the vortex. Since we work with hollow

core, we use $c = 0$. Note that (1.12) and (1.13) depend on a_0 only logarithmically. The behavior of the vortex ring is thus quite insensitive to the exact value of a_0 (expected to be of the order of atomic dimension).

!!TODO!! Life expectancy

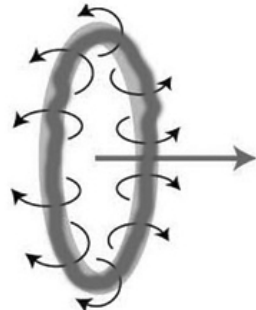


Figure 1.4: Depiction of quantized vortex ring motion

Macroscopic view

Besides NLSE and Vortex filament model, there is also a third, *macroscopic* model in which the individual vortex lines are invisible. On the other side, Helium II is considered as a continuous flow of vortices.

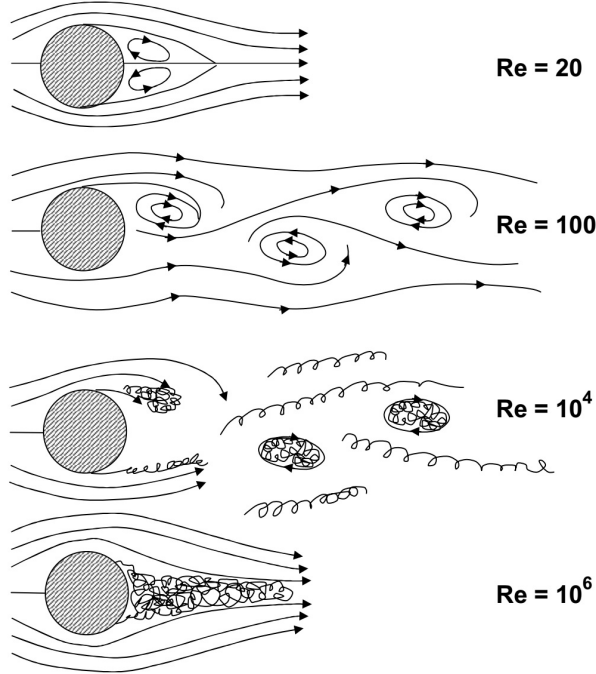


Figure 1.5: transition from laminar to turbulent flow

1.5 Hydrodynamics of superfluid

Such macroscopic model is called the HVBK model and provides a generalization of Landau's two-fluid model equations, including the presence of vortices. The superfluid is treated as a continuum and we can define a macroscopic superfluid vorticity Ω_s , despite the fact that, microscopically, the superfluid velocity field obeys $\nabla \times \mathbf{v}_s = \mathbf{0}$. The downside of this model is its assumption of spatially (not randomly) organized vortices. The common example is a rotating cylinder.

The incompressible HVBK equations for normal and superfluid component, respectively:

$$\frac{\partial \mathbf{v}_n}{\partial t} + (\mathbf{v}_n \cdot \nabla) \mathbf{v}_n = -\frac{1}{\rho} \nabla P - \frac{\rho_s}{\rho_n} S \nabla T + \nu_n \nabla^2 \mathbf{v}_n + \mathbf{F}_{ns}, \quad (1.14)$$

$$\frac{\partial \mathbf{v}_s}{\partial t} + (\mathbf{v}_s \cdot \nabla) \mathbf{v}_s = -\frac{1}{\rho} \nabla P + S \nabla T + \mathbf{T} - \frac{\rho_n}{\rho} \mathbf{F}_{ns}, \quad (1.15)$$

where we have defined:

$$\boldsymbol{\Omega}_s = \nabla \times \mathbf{v}_s, \quad (1.16)$$

$$\mathbf{F} = \frac{B}{2} \hat{\boldsymbol{\Omega}} \times [\hat{\boldsymbol{\Omega}}_s \times (\mathbf{v}_n - \mathbf{v}_s - \nu_s \nabla \times \hat{\boldsymbol{\Omega}})] + \frac{B'}{2} \boldsymbol{\Omega}_s \times (\mathbf{v}_n - \mathbf{v}_s - \nu_s \nabla \times \hat{\boldsymbol{\Omega}}_s), \quad (1.17)$$

$$\hat{\boldsymbol{\Omega}}_s = \boldsymbol{\Omega}_s / |\boldsymbol{\Omega}_s|, \quad (1.18)$$

$$\mathbf{T} = -\nu_s \boldsymbol{\Omega}_s \times (\nabla \times \hat{\boldsymbol{\Omega}}_s) \quad (1.19)$$

$$\nu_s = \frac{\kappa}{4\pi} \log(b_0/a_0) \quad (1.20)$$

Here we can identify the quantities as F (mutual friction force), T (tension force) and ν_s (vortex tension parameter). b_0 is the intervortex spacing and can be estimated as $b_0 = (2\Omega_s \kappa)^{-1/2}$. Note that two-fluid equations by Landau can be achieved by neglecting \mathbf{F} and \mathbf{T} . The HVBK equations have reasonably set the limits:

- $T \rightarrow T_\lambda$: In this case $\rho_s \rightarrow 0$ and the normal fluid equation (1.14) becomes the classical Navier-Stokes equation.
- $T \rightarrow 0$: In this case $\rho_n \rightarrow 0$ so the superfluid equation (1.15) describes a pure superflow. Additionally, taking the classical limit ($\hbar \rightarrow 0$) would take us to the pure Euler equation of inviscid fluid.

The HVBK model has been widely used with success to study the transition to classical or quantum turbulence, for estimations of critical Reynolds numbers and its temperature dependence.

Dynamical similarity of flow

The important role in the behaviour of fluids is taken by the *fluid dimensional numbers*, which are a set of dynamical quantities representing transport phenomena. In purpose to describe Helium-II with correct equations and with the most precision, we have to choose which dimensionless parameters are useful.

- Knudsen number (Kn): This number helps determine whether statistical mechanics or the continuum mechanics formulation of fluid should be used to model the system. Kn is defined as the ratio of the molecular mean free path length λ (the distance of superfluid atom without excitation) to a representative physical length scale D (container size).

If temperature of Helium-II rises above $\approx 1.0\text{ K}$, there is still sufficient amount of normal component and the mean free path of superfluid atoms is much smaller, comparing it with container scale $\lambda \ll D$.

In that case, continuum mechanics could be used as a macroscopic theory for superfluid Helium-II.

- Weissenberg number (Wi): This number is used in the study of viscoelasticity of flow. Wi number indicates the degree of anisotropy generated by the deformation, and is appropriate to describe flows with a constant stretch history, such as simple shear. Wi is usually calculated as a multiplication of shear rate $\dot{\gamma}$ and the relaxation time τ .

Since the relaxation time of Helium-II is relatively small, then $\dot{\gamma}\tau \ll 1$, so the superfluid can be considered as a Newtonian fluid.

- Reynolds number (Re): Let's consider the continuum and newtonian assumptions ($\text{Kn} \ll 1$ and $\text{Wi} \ll 1$), so the fluid can be described by the raw form of Navier-Stokes (N-S) equation of motion. When we take into account also the incompressibility $\nabla \cdot \mathbf{v} = 0$, the N-S reduces itself to its most simplest form, as depicted in (1.14).

In case of stationary flow ($\partial \mathbf{v} / \partial t = 0$), N-S can be rewritten into a dimensionless form. Following these steps, there arises typical values of velocity U and length scale L , at which there is the most significant change in velocity. Re can be expressed as a ratio of inertial and dissipative forces as $\text{Re} = UL\rho/\eta$, where η is the dynamic viscosity of the flow field.

The dimensionless scaling of motion equations in fluid mechanics is called the principle of *dynamic similarity*. Macroscopically it is a phenomenon when comparing two geometrically similar vessels (same shape, different sizes) with the same boundary conditions and the same Reynolds numbers, then the fluid flows will be identical. The derivation of this phenomenon can be directly seen from inspection of the underlying motion equation (1.14), with geometrically similar bodies. In the classical fluid dynamics of ordinary fluids, we use dynamical similarity and scaling arguments for expressing experimental data in terms of Reynolds numbers, drag coefficients, lift, and so on.

The *drag coefficient* C_D is a dimensionless parameter, representing the relation between *drag force* \mathbf{f} and fluid velocity \mathbf{v} , and usually takes the form:

$$C_D \propto v^\alpha, \quad \text{where } \begin{cases} \alpha = -1 & \text{for } \text{Re} \in (0 - 10) \\ \alpha = 0 & \text{for } \text{Re} \in (10^3 - 10^5) \end{cases} .$$

It is very common to plot experimentally measured dependence $C_D(\text{Re})$ for various object past flow:

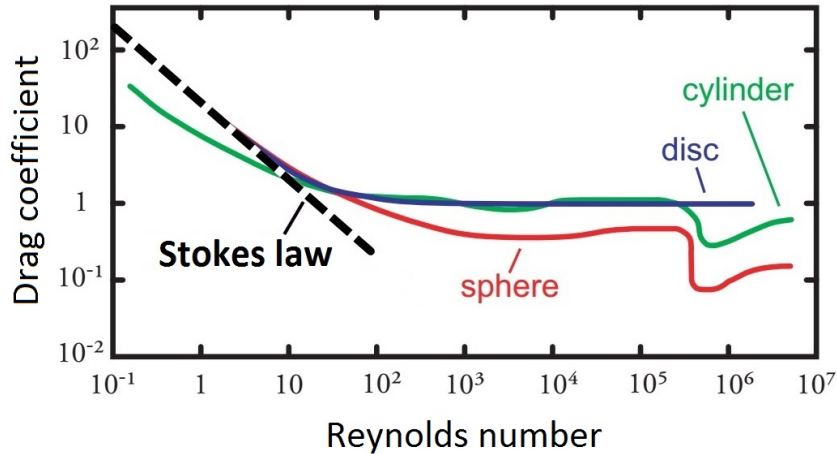


Figure 1.6: Drag coefficients of different objects with changing Reynolds number.

Dynamical similarity argument also leads to the existence of critical Reynolds number, at which the transition to turbulence occurs. Note that since superfluid Helium-II is composed of two fluids, the mentioned applies only on the normal component.

1.6 Oscillatory motion in superfluid Helium-II

In case of oscillating body in classical viscous fluid, described by ordinary Navier-Stokes equation, the typical length scale L is identified as the viscous penetration depth:

$$\delta = \sqrt{\frac{2\eta}{\rho\omega}}, \quad (1.21)$$

where ω is the angular frequency of oscillations. In the high frequency limit, depending on body geometry, the substitution $\delta \rightarrow L$ in Reynolds number formula, is correct and we can calculate an *oscillatory Reynolds number* $\text{Re}_\delta = \delta U \rho / \eta$. The reason for not using the body size is the additional degree of freedom in oscillatory flow (the time period of one oscillation).

Assuming two independent velocity fields \mathbf{v}_n , \mathbf{v}_s in superfluid Helium-II, the above thoughts are applicable for the oscillatory viscous flow of the normal component \mathbf{v}_n . We therefore define in high frequency limit:

$$\delta_n = \sqrt{\frac{2\eta}{\rho_n \omega}}, \quad D_n = \frac{U \delta_n \rho_n}{\eta}, \quad (1.22)$$

We will call the oscillatory Reynolds number for normal component in superfluid Helium-II as a *Donnelly number* D_n .

In low-frequency mode, when $\delta \ll$ oscillating body size L , the Helium-II flow of normal component is fully potential, so it will exhibit a laminar viscous flow. In this case it is shown that the drag coefficient is square-root dependent on oscillation frequency:

$$C_{Dn} \propto \sqrt{\eta \omega} \propto D_n^{-1} \quad (1.23)$$

Since the density of normal component is decreasing with temperature, the critical Donnelly number of normal component shifts to higher numbers:

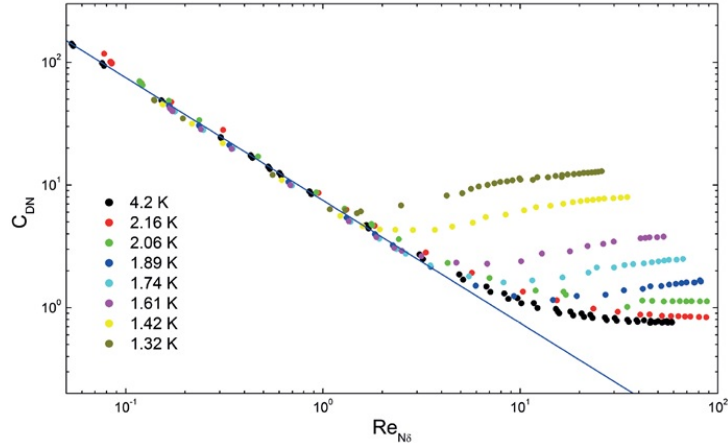


Figure 1.7: Drag coefficients vs Reynolds numbers of normal component. The non-constant behaviour of low-temperature curves (in turbulent mode) are caused due to additional QT in the superfluid component.

For the superfluid component, the drag coefficient C_{Ds} is derived directly from the hydrodynamic description:

$$C_{Ds} = \frac{2F_{drag,s}}{A \rho_s U^2}, \quad (1.24)$$

where A is a surface, dragged by the flow.

1.7 Quantum turbulence

Superfluid turbulence can be viewed as a tangle of vortex lines and can be generated many ways. The first successful try was done using turbulent thermal counterflow by Vinen. Other popular ways to generate turbulence are

The instability leading to the quantized vorticity is amplified by the self-reconnecting property of vortex loops and the critical velocity U_{crit} is expected to scale with frequency as $U_{crit} \propto \sqrt{\omega}$. Hence we define the dimensionless velocity $\hat{U} = U/\sqrt{\omega}$.

A couple of experimental studies in milliKelvin temperatures reported the existence of more critical velocities related with superfluid component flow within single experiment:

- First critical velocity is related with the formation of quantum vortex rings near the surface of oscillating body - possibly forming a thin layer of different hydrodynamic behaviour. Such critical velocity is hard to observe at higher than ultra-low temperature.
- Second critical velocity is a consequence of escaping vortex rings from the oscillator body and forming a superfluid bulk or, eventually, the whole turbulent tangle. Here the sudden raise of drag is observed, usually with hysteresis effect.
- Third critical velocity is the highest critical velocity, which can be observed. The origin of this velocity is hidden in the development of larger quantized vortex structures, which in larger scale become to mimic the classical turbulence. Such velocity is in order \approx m/s and moreover, very likely screened by the influence of the normal component turbulence. Therefore, not likely reachable within experiments reported in this thesis.

When both velocities of Helium II are high enough, we expect the turbulent regime on both sides to be coupled due to mutual friction and contributing to the drag. In such situation, we are forced to use classical hydrodynamic metrics: drag coefficient $C_D = 2F/(A\rho U^2)$ and Donnelly number $D = U\delta/\nu$. Recent researches also hint that both classical turbulent and quantum turbulent regimes can exist separately with low interaction.

Note that all presented approaches are only approximate, since they are neglecting flows near the oscillating body, evaporation processes, sound emissions and other corner-case effects.

2. Experimental Approach

There are many ways how to perform production of quantum turbulence (QT): by an oscillating objects (wire, the tuning fork, the torsionally oscillating disc, etc.) or by a *cocflow* or *counterflow* techniques.

To form the QT we used the tuning fork resonator, driven by alternating source Agilent A33220 and SR830 amplifying lock-in. Signal detection was made using second sound sensors and monitored by LabView software.

All the measurements were performed in a helium cryostat, cooled down to the desired temperatures using a rotary and Roots pump, and stabilized (with errors of a few mK) either manually or using the temperature controller. The working temperatures are from a wide range from a little above T_λ to the lowest (experimentally) possible one $T_{min} \approx 1.26$ K.

2.1 Apparatus

- cryostat
- cooling system
- insert
- resonator

Patova bakalárka

Apparatus:



Figure 2.1: abcd



Figure 2.2: abcd

Insert:

Chamber:

2.2 Generation of QT

From the variety of oscillating candidates we chose the most available and reliable one - the quartz tuning fork. Quartz tuning forks (TF) are commercial piezoelectric oscillators with a well-calibrated resonant frequency. They are usually used as frequency standards in watches or as force sensors in microscopes. Also, TFs have started to be widely used in cryogenic Helium II experiments.

In this work, we used the fork of following dimensions: prongs length $\mathcal{L} = 3.50\text{ mm}$,

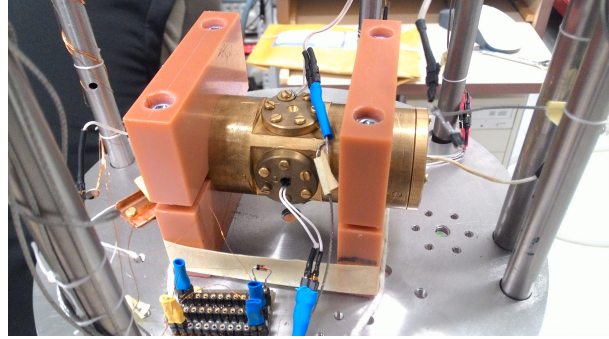


Figure 2.3: abcd

prongs width (perpendicular to the fork plane) $\mathcal{W} = 75\mu\text{m}$, thickness $\mathcal{T} = 90\mu\text{m}$ prongs interdistance $\mathcal{D} = 90\mu\text{m}$. A sketch of the fork architecture is depicted below:

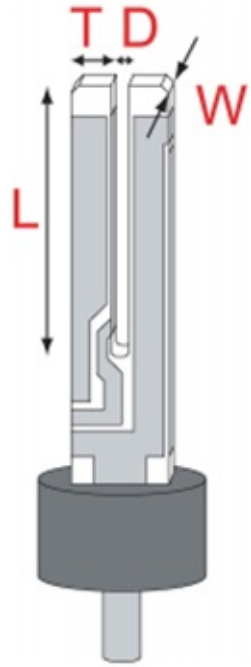


Figure 2.4: Labeled depiction of the tuning forks

There are several achievable resonant modes at which the fork can oscillate. We chose to work with the *fundamental* one at $f_0 = 6.5\text{ kHz}$ and with the first *overtone* one at $f_1 = 40\text{ kHz}$.

The fork is driven by applying an alternate voltage $V(t) \propto e^{i\omega t}$ from a generator to the metallic plates (deposited on fork surface). The piezoelectric effect causes a tension resulting in a force, which is proportional to the applied voltage. In fundamental mode, the fork exhibits an anti-phase oscillating motion of its prongs with a single node. In case of overtone, there would be just two nodes. The fork's flex induces a piezoelectric current $I(t)$ about which is shown its proportionality to the velocity $U(t)$.

The conversion relations between applied $V(t)$, resulting $I(t)$ and mechanical properties $F(t)$, $U(t)$ are:

$$F(t) = \frac{1}{2}a_{rmf}V(t), \quad U(t) = \frac{I(t)}{a_{rmf}}, \quad (2.1)$$

where a_{rmf} is the so-called *fork constant*. This constant can be derived from a fork's geometry, material and an oscillation mode. Usually the formula for this constant is given by a deflection measurement:

$$a_{rmf} = \sqrt{4\pi m_{eff}\Delta f \frac{I}{V}}, \quad (2.2)$$

where m_{eff} id the fork's effective mass and Δf is the measured peak width from the fequency-sweep deflection measurement. In case of our used fork, the effective mass and fork constants for fundamental and overtone modes, respectively:

$$m_{eff} = 1.52 \times 10^{-2} \mu g, \quad a_0 = 0.36 \mu \text{Cm}^{-1}, \quad a_1 = 1.38 \mu \text{Cm}^{-1} \quad (2.3)$$

Other resonators

!!TODO!!

2.3 Measurement methods and Processing

- fork modes - fund, overtone
- frequency sweeps
- amp sweeps

As an observational technique we used the attenuation of second sound, which also serves to mesure the length of vortex line per unite volume L in superfluid component.

It was shown that a pure classical model could explain the observed time decay of line length L . According to this model, superfluid Helium II behaves as a single fluid with a scaled kinematic viscosity μ' . After an initial time interval, the turbulent energy spectrum has the classical Kolmogorov form $E(k) \propto \varepsilon^{2/3}k^{-5/3}$ and thus energy is continually

transferred in a cascade from lower to higher wave numbers. In finite container, the classical theory predicts the time decay of vortex lin density L as:

$$L(t) \propto \frac{(3C_D)^{3/2}}{\sqrt{\mu'}} t^{-3/2} \quad (2.4)$$

3. Simulations

This part of thesis serves as a general description of the **PyVort** codebase, a new platform to simulate quantum vortex rings. The code is written in well commented Python 3, arranged in a modular structure. The primary aim of this chapter is to highlight which module(s) are involved and how they work. In appendix, one can find a table of the parameters (user's options) which can be set in the `config.py` file to run simulation.

At present, we use infinite boundary conditions. Therefore, only closed-loop vortices can be realized in simulation. However, the codebase is flexible and supports the potential implementation of unclosed loops.

3.1 Vortex filament model

The **PyVort** code is based on vortex filament (VF) model, a technique pioneered by Schwarz in the early 1980s [6]. Superfluid vortex filament is represented by a series of mesh points (segments) distributed along the centerline of the filament (**Figure 3.1**). The motion of the whole VF is summed up by the motion of each mesh point.

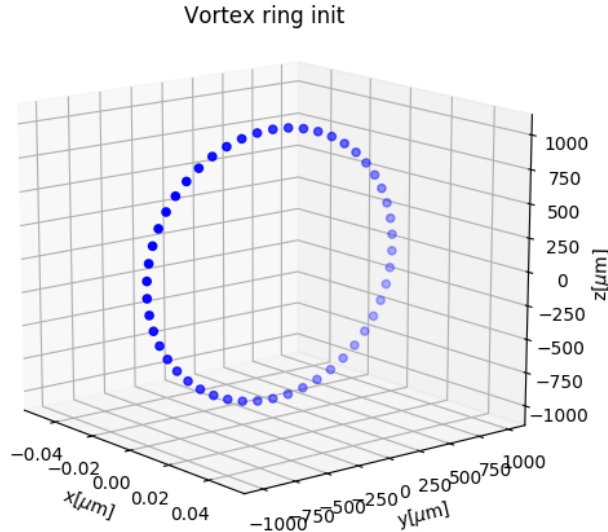


Figure 3.1: Visualisation of vortex ring segments right after their initialisation.

As introduced in Theoretical Background, we define the VF more precisely as a three dimensional curve $\mathbf{s}(\xi, t)$. Here, ξ represent an arc-lengths and t is time. Each segment is given by its coordinates \mathbf{s}_i , direct neighbour indices (previous $(i - 1)$ and next $(i + 1)$). This resolves in a directed digraph of segments, which is a good starting point for the initial data structure.

Next we define the tangent vector \mathbf{s}' , then normal vector \mathbf{s}'' , and the binormal vector $\mathbf{s}' \times \mathbf{s}''$ by taking numerical derivatives. Note $\mathbf{s}' = d\mathbf{s}/d\xi$, and so on. Numerical derivatives are achieved using Finite Differences method, as introduced in next subsection.

Finite differences

In order to properly calculate the numerical derivatives \mathbf{s}' and \mathbf{s}'' , belonging to the directed curve in 3D, we need to use a sophisticated numerical method. At a particular segment with position \mathbf{s}_i , we define the distance to the particle in-front \mathbf{s}_{i+1} as $l_i = |\mathbf{s}_{i+1} - \mathbf{s}_i|$ and the distance to the particle behind \mathbf{s}_{i-1} as $l_{i-1} = |\mathbf{s}_i - \mathbf{s}_{i-1}|$ (**Figure 3.2**). By in-front/behind we refer to the particles next/previous along the filament.

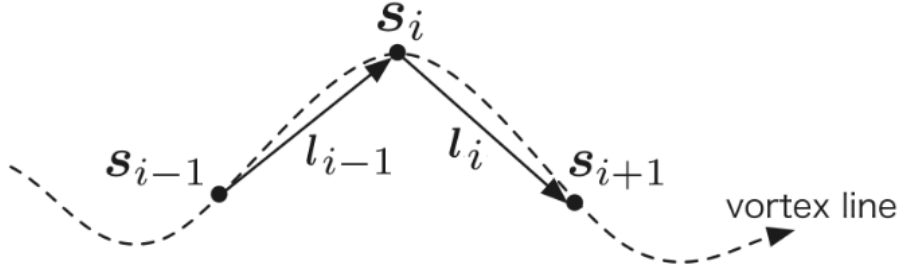


Figure 3.2: Depiction of i -th segment vector and its corresponding lengths. Source: [7]

For accuracy, we approximate all the spatial derivatives \mathbf{s}'_i , \mathbf{s}''_i by a fourth-order finite difference method (FD), which can also account the varying distances along the vortex filament. With this, the first and second derivatives can be obtained based on coordinates of 2 closest neighbours (on each side).

Using FD theorem, we can construct the approximations by taking the Taylor's series expansions. We can then write:

$$\frac{d^n \mathbf{s}_i}{d\xi^n} \approx A_i \mathbf{s}_{i-2} + B_i \mathbf{s}_{i-1} + C_i \mathbf{s}_i + D_i \mathbf{s}_{i+1} + E_i \mathbf{s}_{i+2} \quad \text{for } n \in \{1, 2\} \quad (3.1)$$

Calculation of coefficients A, B, C, D, E can be done using analytical solution of *Vandermonde matrix* inversion. This inversion can be done also numerically, which is a more scalable way of implementation, however, this method often meets with problems when the Vandermonde matrix becomes singular. In code, there is implemented both the analytical solution (closed form) and the solution by inverting the Vandermonde matrix. The closed form works for exactly our form of approximation (3.1), whereas the numerical method works generally for any approximation level.

Biot-Savart discretisation

We denote the static external sources of velocity fields (which can be set in `config.py`) as $\mathbf{v}_{n,ext}$ and $\mathbf{v}_{s,ext}$. The equation of motion for given segment is then given directly by Schwarz's equation(1.11):

$$\frac{d\mathbf{s}_i}{dt} = \mathbf{v}_{s,ext} + \mathbf{v}_{\text{ind}}^{(i)} + \mathbf{v}_{\text{drive}}^{(i)} \quad (3.2)$$

The first difficulty in the VF model comes from the calculation of term \mathbf{v}_{ind} . As we shown previously (1.6), this advection term can be split into the LIA part and a Biot-Savart integral:

$$\mathbf{v}_{\text{ind}}^{(i)} = \mathbf{v}_{\text{LIA}}^{(i)} + \mathbf{v}_{\text{BIOT}}^{(i)} = \frac{\kappa}{4\pi} (\mathbf{s}'_i \times \mathbf{s}''_i) \ln \left(\frac{2\sqrt{l_{i-1}l_i}}{a} \right) + \frac{\kappa}{4\pi} \int_{\mathcal{L}'} \frac{(\mathbf{r}' - \mathbf{s}_i) \times d\mathbf{r}'}{|\mathbf{r}' - \mathbf{s}_i|^3}, \quad (3.3)$$

where l_{i-1} and l_i are the arc lengths of the curve between points \mathbf{s}_{i-1} and \mathbf{s}_i and between \mathbf{s}_i and \mathbf{s}_{i+1} respectively, and \mathcal{L}' is the original vortex line without the two segment lines between \mathbf{s}_{i-1} and \mathbf{s}_{i+1} .

Using the segment discretisation, the Biot-Savart integral can be rewritten [7] into the sum of single-line contributions (**Figure 3.3**) between each j -th and $j+1$ -th segment (except for the ones attached to the i -th point):

$$\mathbf{v}_{\text{BIOT}}^{(i)} \approx \frac{\kappa}{4\pi} \sum_{j \notin \{i-1, i\}} \frac{(R_j + R_{j+1})(\mathbf{R}_j \times \mathbf{R}_{j+1})}{R_j R_{j+1} (R_j R_{j+1} + \mathbf{R}_j \cdot \mathbf{R}_{j+1})}, \quad (3.4)$$

where $\mathbf{R}_j = \mathbf{s}_j - \mathbf{s}_i$ and $\mathbf{R}_{j+1} = \mathbf{s}_{j+1} - \mathbf{s}_i$ are the relative vectors from the given point.

Note that, if one takes in account the Biot-Savart law for N mesh points, the computational time is proportional to $\mathcal{O}(N^2)$, while, if one uses just the LIA term, it is only $\mathcal{O}(N)$. Numerical simulations based on Biot-Savart are therefore significantly more computationally expensive, even with the speed of today's computers.

One way to get around this difficulty is to update the LIA term. In this method we neglect completely the non-local Biot-Savart integral and keep just the local term. This is typically done with a minor adjustments within the log term:

$$\mathbf{v}_{\text{LIA}}^{(i)} = \frac{\kappa}{4\pi} (\mathbf{s}'_i \times \mathbf{s}''_i) \ln \left(\frac{2R_i}{a} \right), \quad (3.5)$$

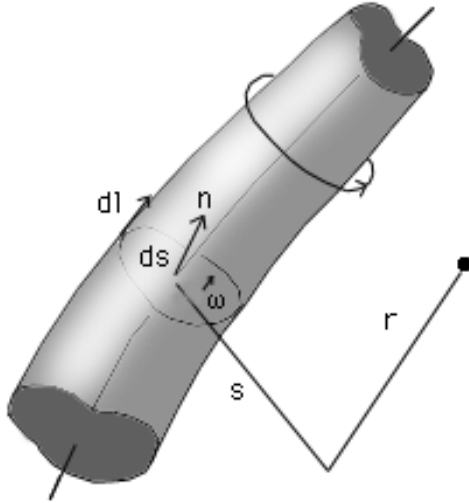


Figure 3.3: An infinitesimal contribution of a j -th segment line between two points \mathbf{s}_j and \mathbf{s}_{j+1} at a given point \mathbf{r} . Source: Internet

where R_i is a filament length scale - may be taken [6] as a local curvature of i -th segment: $R_i = 1/|\mathbf{s}''_i|$. Updated LIA is a very convenient approximation and works very well for calculating the motion of a single vortex ring.

State definition

In code, a single vortex ring object is represented using the `class` structure. This structure is updated after each time step. We will call it as a *state* of the vortex ring and it is defined (and initialised) with following properties:

- shape - a dictionary of three parameters: ring center coordinates $[x_c, y_c, z_c]$, radius R and the direction of desired motion $\{x, y, z\}$ (three possible axis)
- velocity - the actual velocity magnitude of vortex ring center $|\mathbf{v}_c|$
- number of active segments - number of segments N the vortex ring is composed of
- segments - an array of all segments, each one with following attributes:
 - active - a logical value whether a particular segment should be considered as a part of vortex object
 - coordinates - an array of segment coordinates $\mathbf{s}_i = [x_i, y_i, z_i]$
 - previous/next neighbour - array localisation indices of the *previous* ($i-1$) and the *next* ($i+1$) segment within the context of the directed vortex

- tangent/curvature - a tangential and normal vectors \mathbf{s}'_i and \mathbf{s}''_i
- LIA velocity - a self-induced velocity $\mathbf{v}_{\text{LIA}}^{(i)}$ driven by the local curvature.
- BIOT velocity - a self-induced velocity driven by the farther segment lines of the vortex ring $\mathbf{v}_{\text{BIOT}}^{(i)}$
- Drive velocity - a velocity given by the mutual friction force $\mathbf{v}_{\text{drive}}^{(i)}$
- Full velocity - the sum of external sources $\mathbf{v}_{s,\text{ext}}$, LIA velocity $\mathbf{v}_{\text{LIA}}^{(i)}$, BIOT velocity $\mathbf{v}_{\text{BIOT}}^{(i)}$ and the drive velocity $\mathbf{v}_{\text{drive}}^{(i)}$, resulting in $d\mathbf{s}_i/dt$

The proper initialisation of the *state* in the very beginning of simulation includes the following steps:

1. an input from user: *center*, *radius* and *direction*
2. the gradual initialisation of neighbour indices (to an i -th element in segment array will be assigned $i - 1$ index as the *previous* and $i + 1$ index as the *next* neighbour index)
3. Calculation of all \mathbf{s}' and \mathbf{s}'' using Finite differences method
4. Calculation of all segment velocities using motion equations and their approximative forms
5. Calculation of the center velocity by taking the mean of all segments' full velocities in corresponding direction

3.2 Time evolution

Now when we defined and ran all the necessary calculations leading to the quantum vortex ring's *state* fulfillment, we can start to propagate it in time.

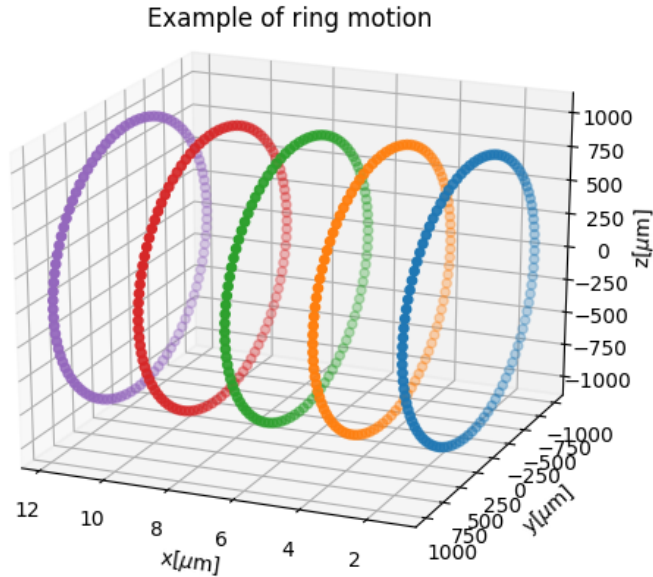


Figure 3.4: Example of a moving vortex ring

Time stepping

Time evolution is based on an explicit iterative method: the fourth-order Runge-Kutta (RK4) scheme. When we consider the Schwarz's equation $\frac{ds_i}{dt} \equiv \mathbf{v}_{\text{full}}^{(i)}$, the stepping algorithm is given as:

$$\mathbf{s}_i(t + dt) = \mathbf{s}_i(t) + \frac{dt}{6}(\mathbf{v}_1^{(i)} + 2\mathbf{v}_2^{(i)} + 2\mathbf{v}_3^{(i)} + \mathbf{v}_4^{(i)}), \quad (3.6)$$

where dt is the time step and the velocities $\mathbf{v}_1^{(i)}, \mathbf{v}_2^{(i)}, \mathbf{v}_3^{(i)}, \mathbf{v}_4^{(i)}$ are the induced velocities of partial steps:

$$\mathbf{v}_1^{(i)} = \mathbf{v}_{\text{full}}^{(i)}(\mathbf{s}_i, t), \quad (3.7)$$

$$\mathbf{v}_2^{(i)} = \mathbf{v}_{\text{full}}^{(i)}(\mathbf{s}_i + \mathbf{v}_1^{(i)} dt/2, t + dt/2), \quad (3.8)$$

$$\mathbf{v}_3^{(i)} = \mathbf{v}_{\text{full}}^{(i)}(\mathbf{s}_i + \mathbf{v}_2^{(i)} dt/2, t + dt/2), \quad (3.9)$$

$$\mathbf{v}_4^{(i)} = \mathbf{v}_{\text{full}}^{(i)}(\mathbf{s}_i + \mathbf{v}_3^{(i)} dt, t + dt) \quad (3.10)$$

Lower-order schemes such as basic Euler method is also implemented in code, however, not recommended to use. More on this is discussed in Results part of thesis.

The time step dt is chosen so that the vortex ring cannot move faster than a 1% of its size in a single step. As we will see later in Results, in case of vortex rings with changing radius, the time step dt has to be iteratively changing after each break of the above rule:

$$dt \leftarrow \frac{0.01R}{|\mathbf{v}_c|} \quad (3.11)$$

3.3 Re-segmentation of vortex

To obtain the most realistic simulation (to catch effects on any length scale), the natural tendency would be to set the resolution parameter δ as low as possible. However, the CPU time cost rises rapidly as the number of segments N increases, so there is need to find the best trade-off.

As the distance between neighbouring segments is compressed/enlarged with time due to the physics and numerical inaccuracies, there is need for remove/add segments (*re-segment*) in order to conserve the vortex resolution δ . The closeness (in terms of arclength) of neighbouring segments is therefore measured after each simulation time-step.

We used the simplest re-segmenting criteria - keeping an approximately *uniform distance* between the segments. To ensure this, two boundary conditions were implemented:

1. The segment \mathbf{s}_{j+1} would be removed if:

$$|\mathbf{s}_{j+1} - \mathbf{s}_j| < \delta_{\min}, \quad (3.12)$$

where δ_{\min} is the minimal distance between two segments. Also, the segment \mathbf{s}_j would take place somewhere between \mathbf{s}_{j-1} and \mathbf{s}_{j+2} so that it will conserve the

curvature of vortex. Such result can be obtained using any spline interpolation along nearest neighbours. We worked with 3D local spline using 4 points (in our context they would be \mathbf{s}_{j-2} , \mathbf{s}_{j-1} , \mathbf{s}_{j+1} , \mathbf{s}_{j+2}) and create another 11 interpolated knots. Consequently, the new position of \mathbf{s}_j will sit on the 6-th (the middle one) knot and also.

2. In a similar manner, we add a new segment \mathbf{s}_{new} between \mathbf{s}_j and \mathbf{s}_{j+1} if:

$$|\mathbf{s}_{j+1} - \mathbf{s}_j| > \delta_{\max}, \quad (3.13)$$

where δ_{\max} is the maximal allowed distance between two segments.

This method keeps all the distances along the vortex roughly in the range $\delta \in \langle \delta_{\min}, \delta_{\max} \rangle$ and also keeps the geometrical properties.

Real-time tests

After each time step is done, a few tests are performed, to ensure that vortex itself is behaving according to our expectations. The tests are following:

- Length test - This test calculates the vortex circumference as $l = \sum_j |\mathbf{s}_j - \mathbf{s}_{j+1}|$ and compare it with the theoretical one $2\pi R$. If the deviation from the theoretical value is too high $> 1\%$, the segments are noisy and the process is killed. In case of deviation below $< -1\%$, there is clearly too less segments and resegmentation is called.
- Segmentation test - Here we check the value $l_j |\mathbf{s}_j - \mathbf{s}_{j+1}|$ for each j and ask whether $l_j \in \langle \delta_{\min}, \delta_{\max} \rangle$. If not, resegmentation is called.
- Smallness test - If the vortex ring radius would decrease below $R < \delta_{\min}$, the ring is deleted from the simulation.

3.4 Future implementations

To make Pyvort a full-fledged quantum vortex simulation, there should be implemented following improvements:

Complexity speedup

Recent numerical research presented [8] a new numerical method to compute the evolution of vortex filament. The method is based on an N-body cosmological simulation by Barnes and Hut [9], a *tree algorithm* which considerably speeds up the calculation of Biot-Savart integrals - computational cost scales as $\mathcal{O}(N \log(N))$ rather than N^2 . Properties of the tree method was tested for a variety of vortex configurations, ranging from simple vortex rings to a counterflow vortex tangle and compared with the LIA approac and the exact Biot-Savart's law.

Implementation of such algorithm is not easy, but definitely worth for the speed-up property.

Re-connection process

If any lines of two vortices (or even the single one) become very close, the filaments can re-connect, changing the topology of the system. Many researchers experimentally reported this is happening and also found analogies with vortex dynamics in the Navier–Stokes equation.

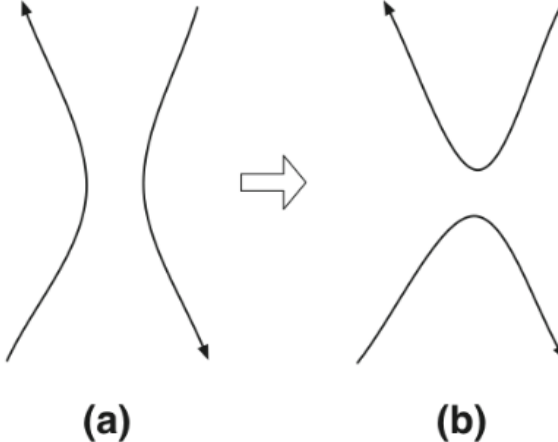


Figure 3.5: Reconnection of quantized vortices. (a) Two vortices before reconnection, about to contact each other. (b) The new vortices after reconnection.

The VF model itself cannot describe the reconnection process because the vortex core structure is neglected. Hence, some artificial procedures must be introduced to simulate such process. For instance, when two vortices approach within a critical distance δ_{\min} , we will artificially reconnect the vortices.

The main criteria for reconnection is that the total length (this is corresponding with

energy) will decrease. Self-reconnections (e.g. caused by a twist of vortex) would be treated in the same way. Since reconnection involves only antiparallel vortices, one has to check using the inner product whether two vortices could physically reconnect or not.

High-order tests

Once the code of interacting vortex filaments is developed, the analysis of all that data has to be improved. The simplest measurable quantity is the total length of all vortex lines. In a finite volume this would be $L = (1/V) \int d\xi$ for the vortex line per unit volume.

Of course, there can be defined more complicated metrics, measuring the isotropy of the vortex tangle. One of them is the length of line projected along a given vector $\hat{\mathbf{r}}$, give as:

$$J(\hat{\mathbf{r}}) = \frac{1}{VL} \int_{\mathcal{L}} \sqrt{1 - (\mathbf{s}'(\xi) \cdot \hat{\mathbf{r}})^2} d\xi \quad (3.14)$$

4. Results (15 pgs)

4.1 Drag force graphs

Fundamental:

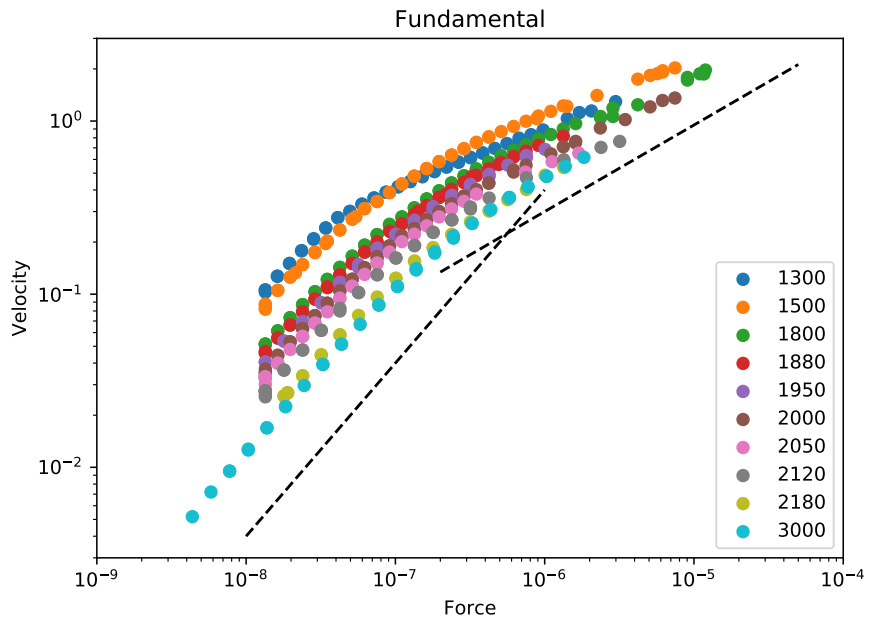


Figure 4.1: Velocity against force

Overtone:

Fundamental drag coefficient:

Overtone drag coefficient:

4.2 Universal Scaling

Fundamental Donnelly:

Overtone Donnelly:

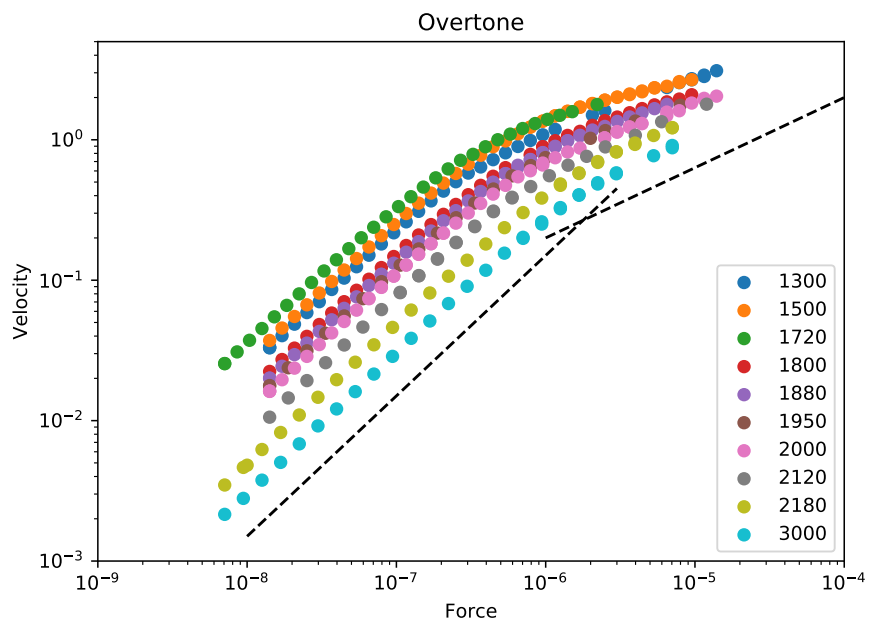


Figure 4.2: Velocity against force

4.3 Flow phase diagram

Fundamental phase diagram:

Overtone phase diagram:

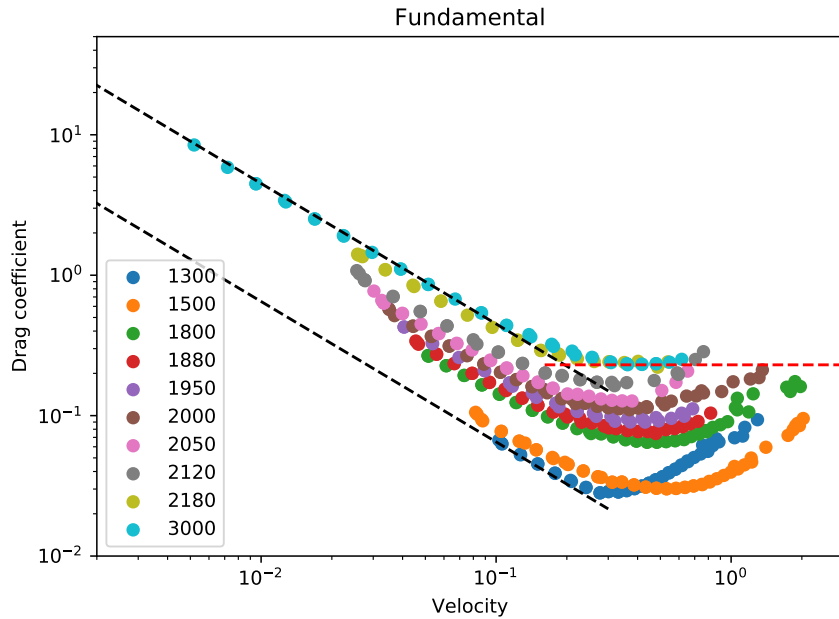


Figure 4.3: Drag coeff against velocity

4.4 Simulation experiments

- does num segments affect the initial ring velocity?
- does energy (and velocity) changes if Quantum=False?
- for a given R and euler method, what is the life of stability for various num segments
- when is it good to resegment?
- which config leads to the death of the ring for various R
- measure death time and distance for various R

4.5 Vortex ring

- compare rings with various radii
- theoretical vs simulation velocity / range
- stability tests
- initialisation

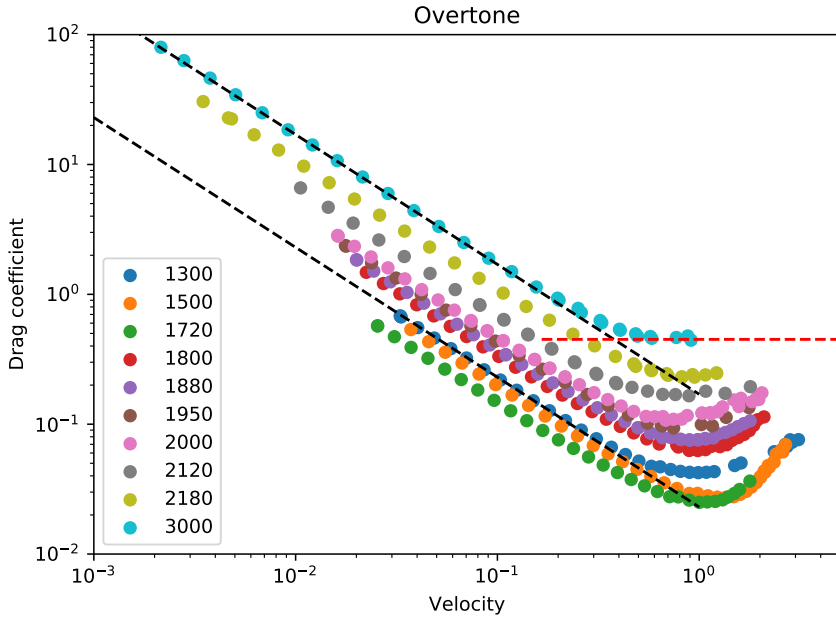


Figure 4.4: Drag coeff against velocity

- movement, decreasing radius
- comparison with theory

All presented measurements and results were done in purpose of setup the `config` file. We performed a tests with physical motivation and tests focused on precision and stability. With presented findings, there should be ensured the correctness and stability of any further high-scale simulation.

Frictionless test

In case of zero temperature $T = 0\text{ K}$, there should be no *normal component* in superfluid He-II and therefore also no mutual friction. In such case, velocity and energy of vortex ring is conserved due to the lack of energy dissipation processes.

We plotted in **Figure 10** the ring velocity $|\mathbf{v}_c|$ and energy evolving in time, for the case of $T = 0$ and $T = 1.5\text{ K}$. We tested the mutual friction effect during 1000 time-steps (*epochs*) with varying dt .

As we see, at $T = 0\text{ K}$ the velocity and energy is conserved even after 1000 epochs of simulation. In case of $T > 0$, energy is falling down as expected, whereas the velocity

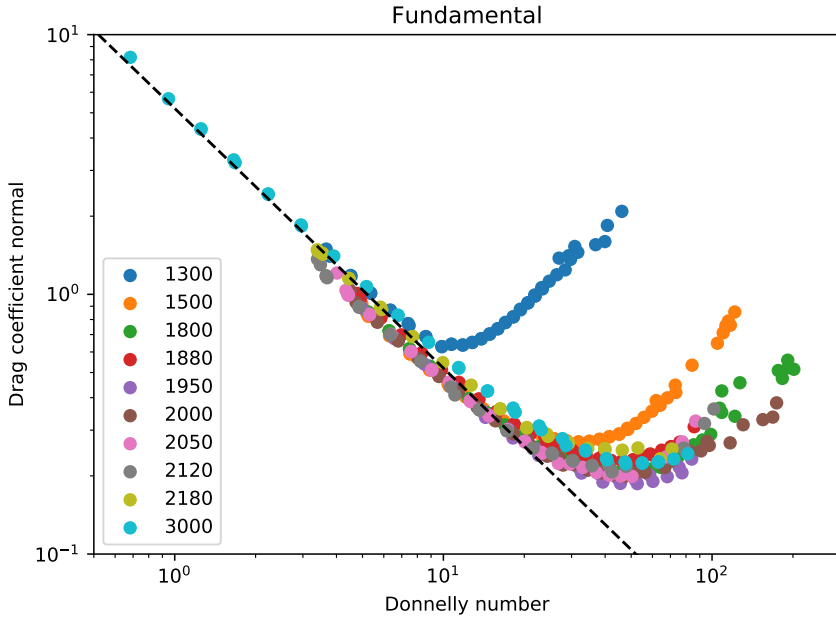


Figure 4.5: Donnelly num against velocity

is increasing. This increase is physically well-explained by the fact that the radius is decreasing with time (1.13), also due to mutual friction.

Velocity precision test

Our first velocity test compares the various approaches how can the ring velocity $|\mathbf{v}_c|$ be calculated. Here, we recognize between four approaches, based on its theoretical motivation, computational complexity and precision:

- LIA (??): motivated, cheap, not precise
- LIA + BIOT (?? + ??): motivated, but expensive
- updated LIA (??): not well motivated, but cheap and precise
- Theoretical (1.13): well motivated and precise

Of course, the theoretical velocity (1.13) is taken as a baseline that other velocities are compared with. All velocities were evolved and measured during 5000 epochs (time steps), as we see in **Figure 11**.

As we see, the (LIA + BIOT) velocity grows much faster than it should according to

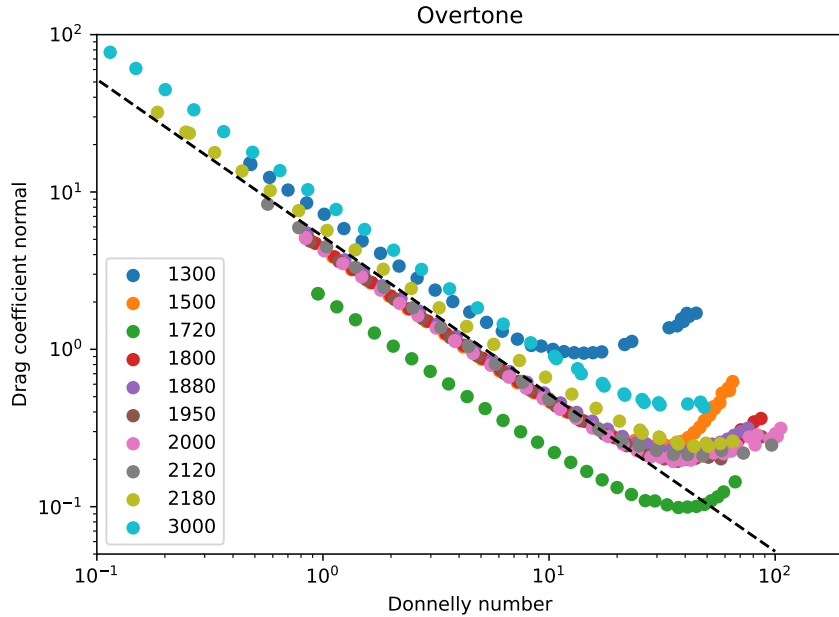


Figure 4.6: Donnelly num against velocity

theory. Therefore, for all further measurements we used the updated LIA velocity (LIA^*) due to its precision and speed.

Velocity convergence test

Next, we investigated the magnitude of ring velocity $|\mathbf{v}_c|$ for various resolutions $\delta \in \langle 50, 200 \rangle \mu\text{m}$, immediately after initialisation and then after 100 epochs. Ring radius was set at $R = 1000 \mu\text{m}$, so the number of discretisation points was given by R and δ as $N \approx 2\pi R/\delta \in \langle 30, 120 \rangle$.

We see in **Figure 12** the expected convergent behaviour of both measured velocities in an area of good resolutions. Below $\delta < 100 \mu\text{m}$, the velocities are enough convergent (corresponding to ≈ 60 number of segments), which gives us the upper boundary.

Even if it is intuitive that good resolutions lead to more stable velocities, the high number of vortex segments worsens the stability of simulation in time. Therefore, we propose also a lower boundary δ_{\min} , ensuring the stability, in a following test.

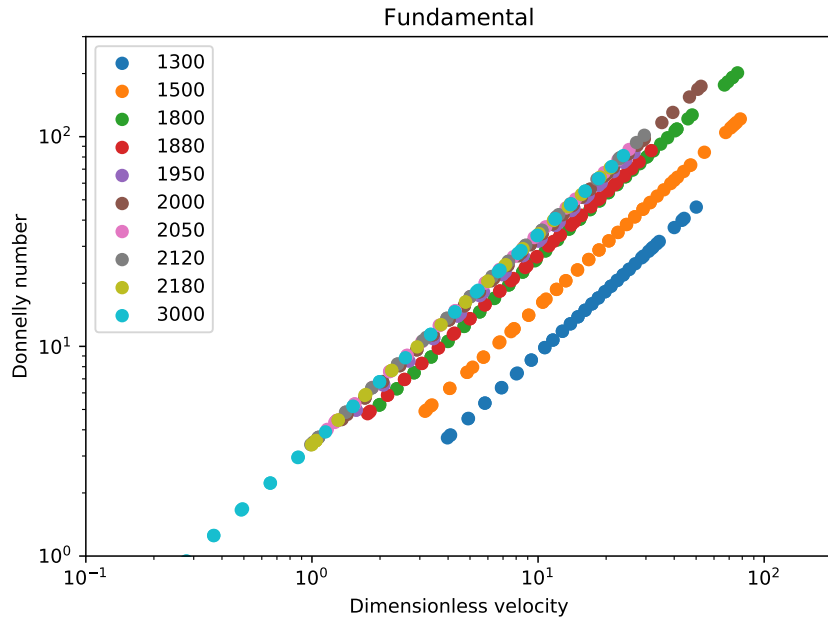


Figure 4.7: Donnelly num against dimless velocity

Stability test

Stability of simulation was measured for three values of vortex radius $R \in \{500, 1000, 2000\} \mu\text{m}$ using *Euler* and *RK4* stepping in various resolutions. In all cases, the stability is described by the number of reached epochs, which was determined by the violation of length condition - the vortex circumference cannot deviate more than 1% from the geometrical value $2\pi R$.

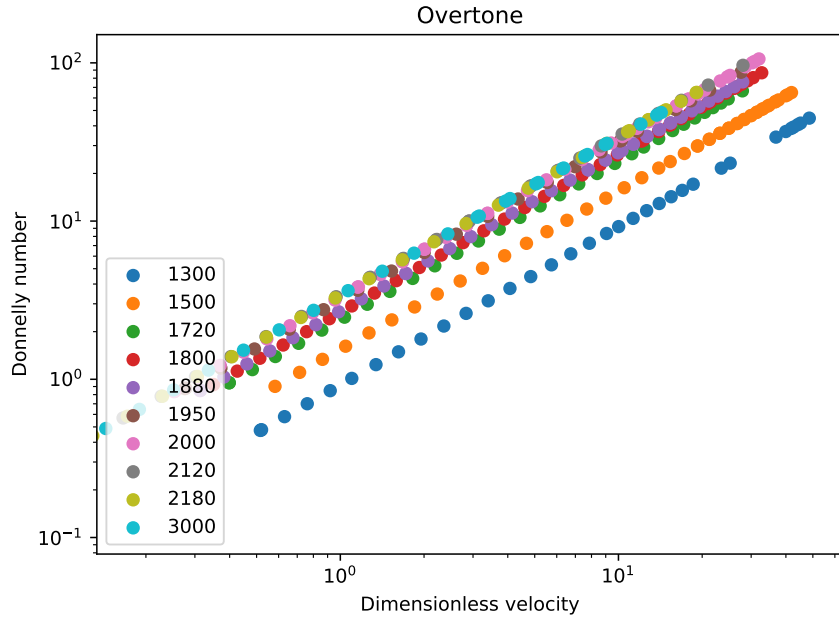


Figure 4.8: Donnelly num against dimless velocity

Euler method seems to be instable for whatever resolution (**Figure 13**). Therefore it is useful only for test purposes. We recommend to use a way more stable method RK4 in a real high-scale simulation:

The plot in **Figure 14** suggests the minimal resolution to be at least $\delta > 30\mu\text{m}$. This boundary is still quite conservative, since the radius of vortex is decreasing in time (see Appendix part), so the resegmentation will happen. Resegmantation processes heavily help the simulation to be stable (deletes any forwarding numerical errors).

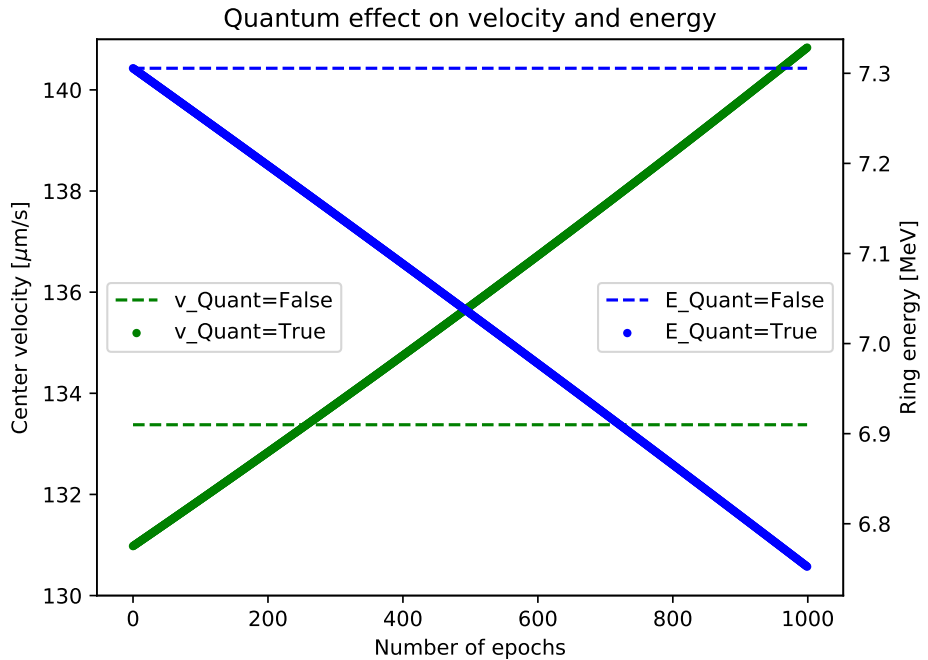


Figure 4.9: Dashed curves show the constant behaviour for temperature $T = 0$), full lines the dissipation process for $T = 1.5\text{K}$. On x axis, we plot the number of epochs (time steps) the vortex ring ran over and on y axis the velocity of ring center $|\mathbf{v}_c|$.

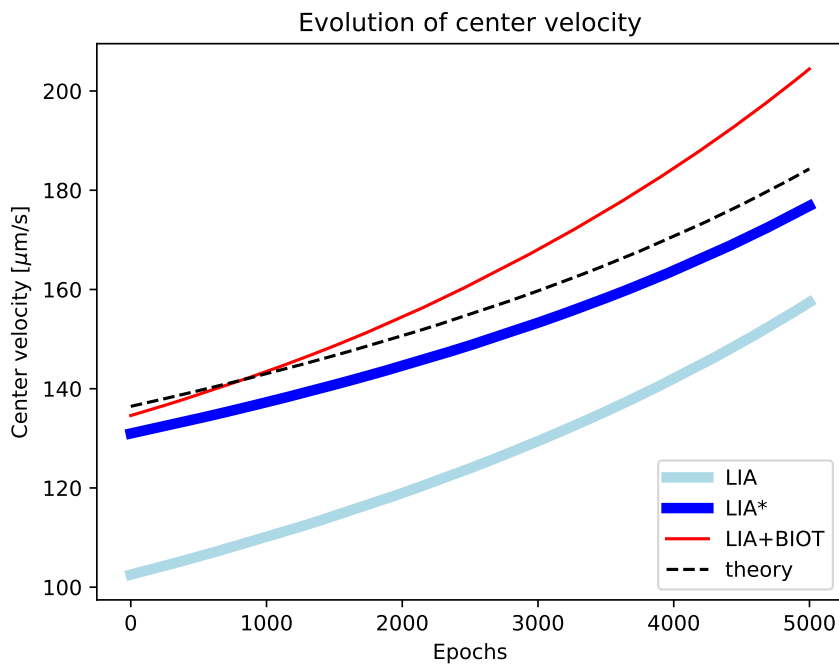


Figure 4.10: Comparison of all implemented velocity approaches (full lines) with the theoretical one (black dashed line). On x axis, we plot the number of epochs (time steps) the vortex ring ran over and on y axis the velocity of ring center $|\mathbf{v}_c|$.

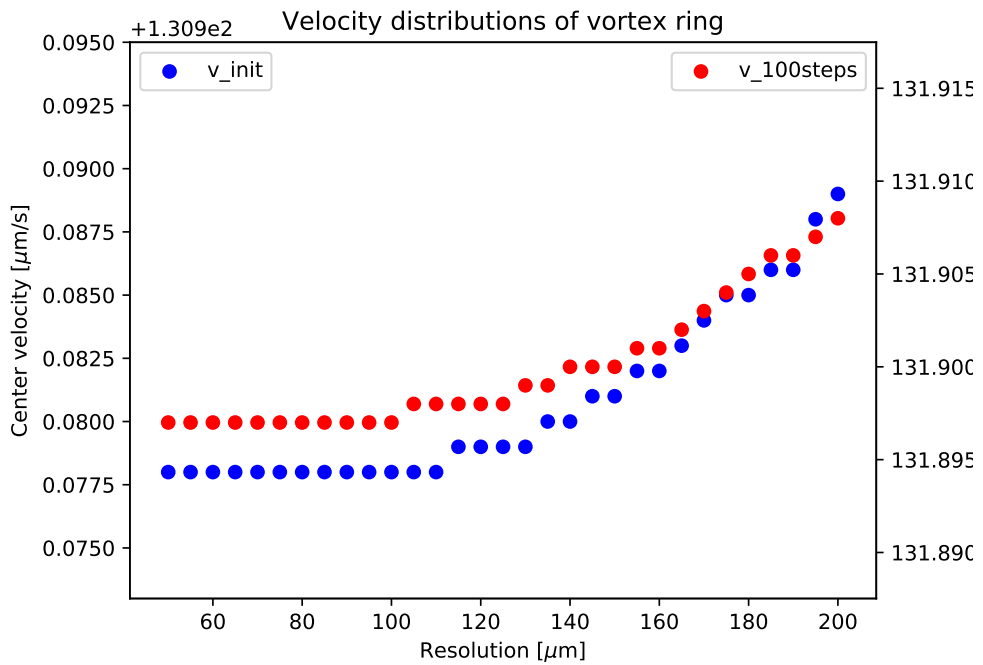


Figure 4.11: On x axis, we plot the resolutions δ and on y axis the velocity of ring center $|\mathbf{v}_c|$. Blue dots - initial ring velocities, Red dots - ring velocities after 100 epochs.

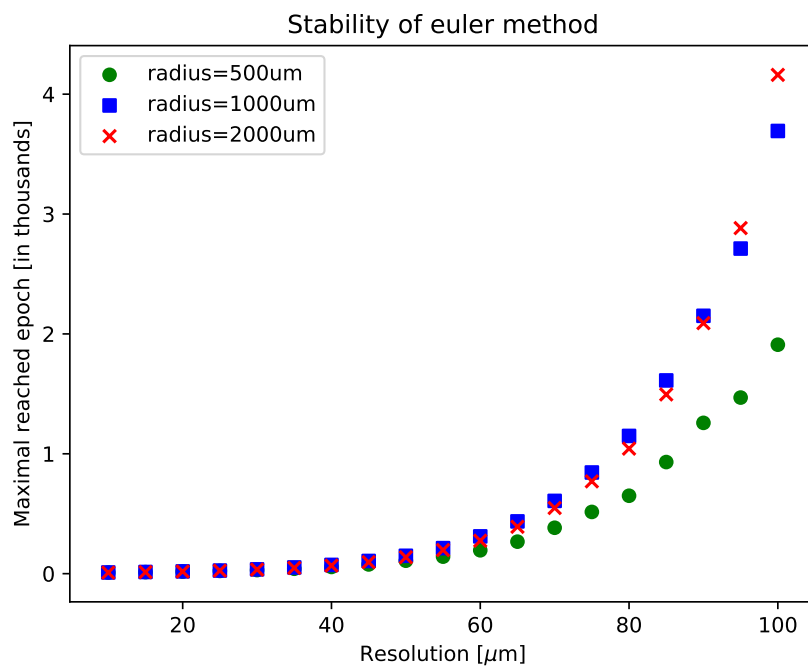


Figure 4.12: Maximal reached epoch (time step) with Euler method till the simulation was killed by violating the length condition, for various radii R and resolutions δ .

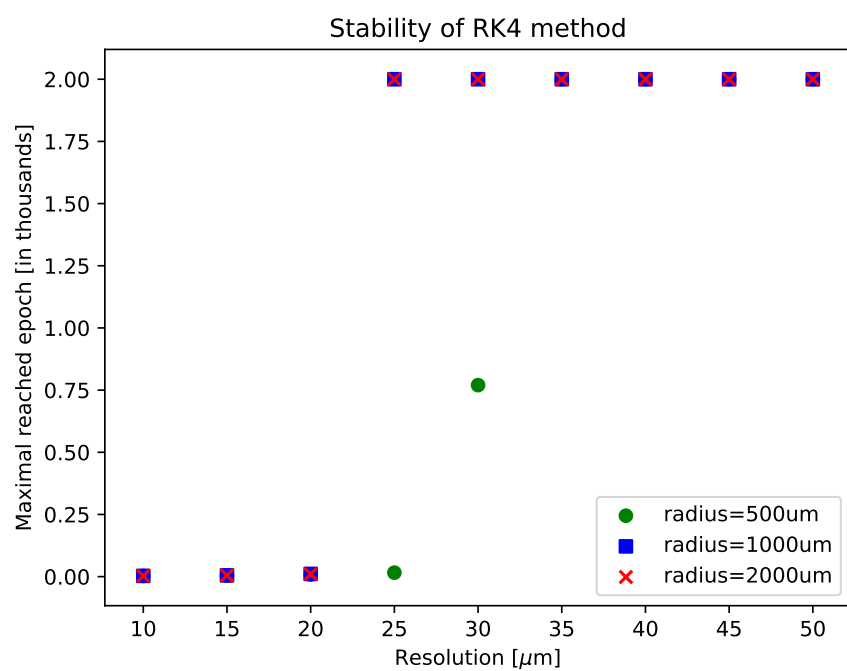


Figure 4.13: Maximal reached epoch (time step) with RK4 method till the simulation was killed by violating the length condition, for various radii R and resolutions δ . A threshold is set on 2000 epochs.

5. Conclusions (2 pgs)

- summarize mainly what have we done
- repeat motivations and goals
- list of achievements
- list of failures
- list of improvements
- last words

In this work, we proposed an effective numerical method to compute the time evolution of vortex ring in superfluid He-II. VF's performance was improved by neglegcting the Biot-Savart integral and updating the LIA calculation instead (??). Simulation well replicates the physical processes and performs sufficient stability when using testing vortex ring of radius $R \in \langle 500, 2000 \rangle \mu\text{m}$ in resolution $\delta \in (60 - 100) \mu\text{m}$.

6. Appendix

To run the code, there has to be installed only Python 3 (with various libraries) on any OS. All the Python code can be found in the directory `src/`. The entire project is open-source and can be found as a public GitHub repository. Pull requests of any further development would be definitely appreciated.

Here we briefly present a few visualisations of observed instabilities and physical processes.

Instability in good resolution

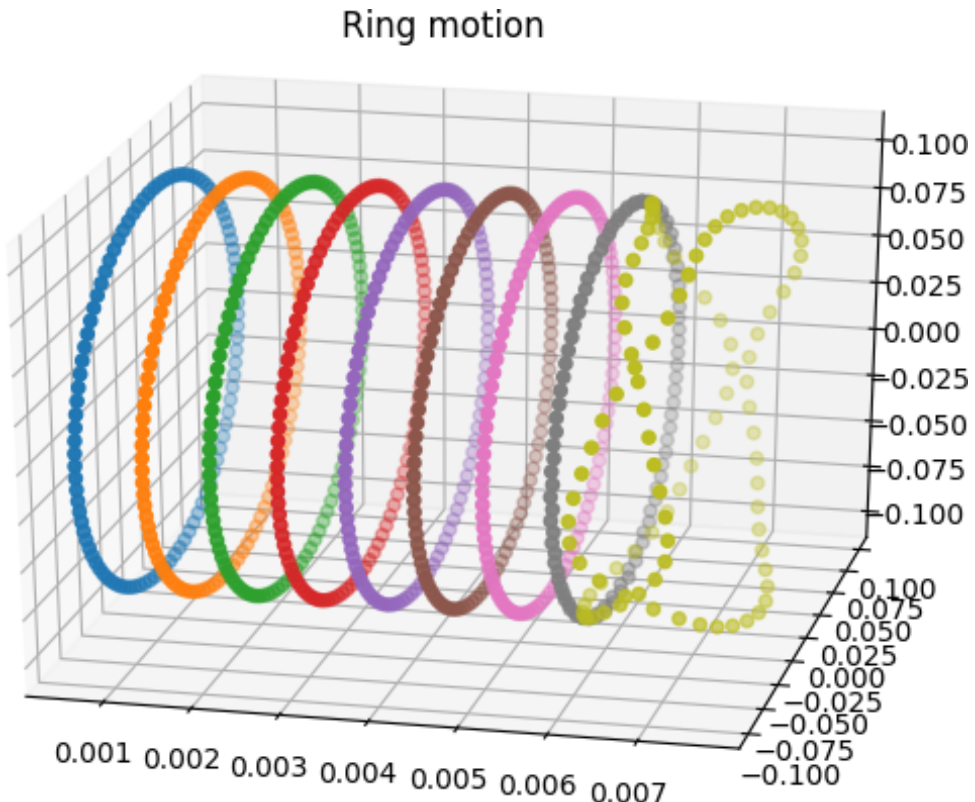


Figure 6.1: A graphical example of ring instability when Euler stepping was used with good resolution (small δ). Ring is moving from the left side to the right with exponentially forwarding error.

Noisy instability in worse resolution

Ring instability

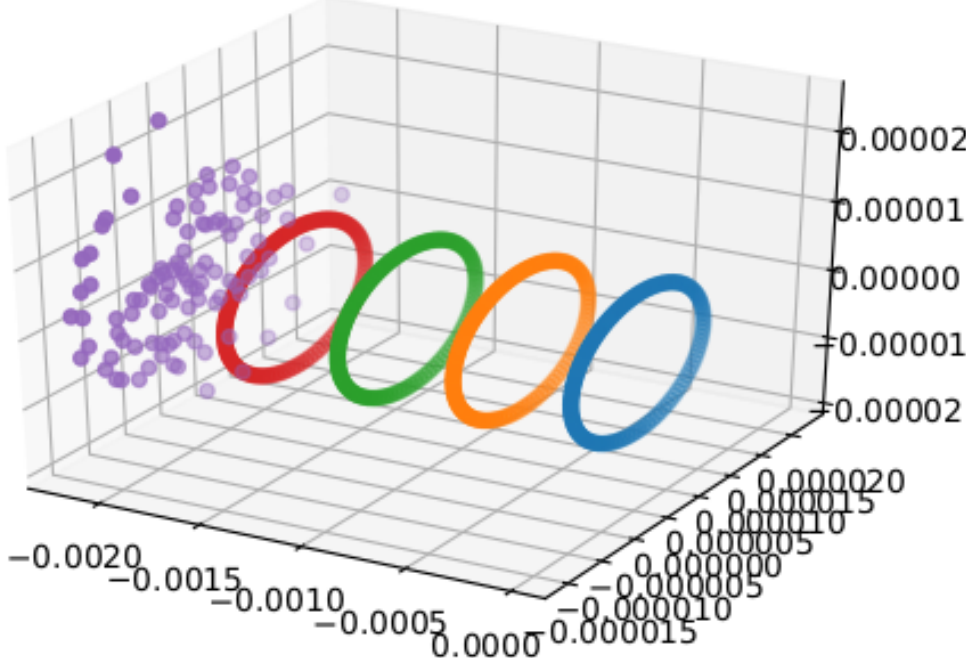


Figure 6.2: Another example of ring instability due to forwarded numerical error using Euler stepping. In this case, resolution δ is higher (worse resolution), so the instability itself is much more noisy.

Mutual friction effects

Also, we present one of the bigger simulations (**Figure 17**) we tested. After we set the ring radius $R = 1000\mu\text{m}$, resolution $\delta = 60\mu\text{m}$ (resulting in around ≈ 100 mesh points), re-segmentation boundaries $\delta_{\min} = \delta/2 = 30\mu\text{m}$, $\delta_{\max} = 2\delta = 120\mu\text{m}$, the updated LIA calculation, RK4 stepping method and a temperature $T = 1.5\text{K}$, we obtained a stable simulation of vortex ring with a decreasing radius. More on particular physical processes can be found in [?].

Ring motion

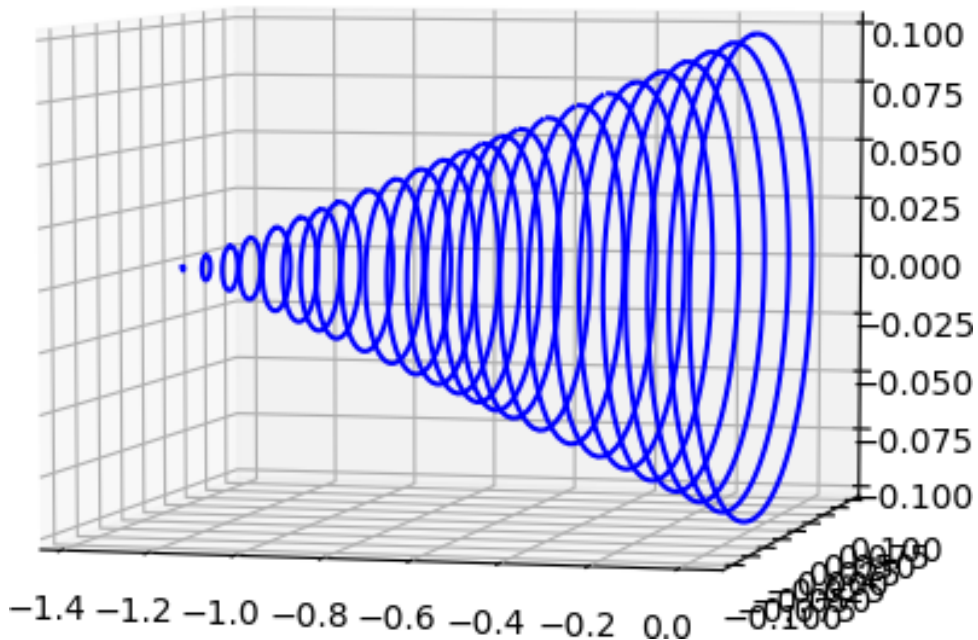


Figure 6.3: Here, a vortex ring is moving to the left, its energy is dissipating due to the mutual friction and therefore, the radius is decreasing in time. The ring re-segmented itself a few times (due to the violation of δ_{\min} condition and died (the simulation was stopped) when the length error was too high.

Bibliography

- [1] KAPITSA, P. *The Super-Fluidity of Liquid Helium II*. Nature **141**, 74 (1938)
- [2] TONG, D. *Statistical physics*. University of Cambridge Part II
- [3] TISZA, L. *The viscosity of liquid helium and the Bose-Einstein statistics*. Comptes Rendus Acad. Sciences, **207**:1186-1189 (1952)
- [4] LANDAU, L.D. and LIFSHITZ, E.M. *Fluid Mechanics*, Second English Edition. Pergamon Books Ltd., (1987). ISBN 0-08-033933-6
- [5] LANDAU, L.D. *The theory of superfluidity of helium II* J. Phys. USSR, Vol. **11**, 91 (1947)
- [6] SCHWARZ, K.W. *Three-dimensional vortex dynamics in superfluid He 4: Homogeneous superfluid turbulence* Phys Rev B, Vol. **38**, 4 (1988)
- [7] TSUBOTA, M., FUJIMOTO, K., YUI S. *Numerical Studies of Quantum Turbulence*. Journal of Low Temp Phys, 188 (2017)
- [8] BAGGLEY, A.W., BARENGHI, C.F. *Tree Method for Quantum Vortex Dynamics*. Journal of Low Temp Phys, 166 (2012)
- [9] BARNES, J., HUT, P. *A hierarchical $O(N \log N)$ force-calculation algorithm*. Nature, **324**, 446 (1986)